Hindawi Publishing Corporation
International Journal of Photoenergy
Volume 2015, Article ID 349030, 8 pages
http://dx.doi.org/10.1155/2015/349030

Research Article

Synthesis, Characterization, and Electronic Structure Studies of Cubic $Bi_{1.5}ZnTa_{1.5}O_7$ for Photocatalytic Applications

Ganchimeg Perenlei,[1] Jose A. Alarco,[1,2] Peter C. Talbot,[1,2] and Wayde N. Martens[1]

[1]*Chemistry, Physics and Mechanical Engineering School, Science and Engineering Faculty, Queensland University of Technology, Brisbane, QLD 4001, Australia*
[2]*Institute for Future Environments, Science and Engineering Faculty, Queensland University of Technology, Brisbane, QLD 4001, Australia*

Correspondence should be addressed to Wayde N. Martens; w.martens@qut.edu.au

Received 16 May 2015; Revised 21 September 2015; Accepted 4 October 2015

Academic Editor: Mohammed Ashraf Gondal

$Bi_{1.5}ZnTa_{1.5}O_7$ (BZT) has been synthesized using an alkoxide based sol-gel reaction route. The evolution of the phases produced from the alkoxide precursors and their properties have been characterized as function of temperature using a combination of thermogravimetric analysis (TGA) coupled with mass spectrometry (MS), infrared emission spectrometry (IES), X-ray diffraction (XRD), ultraviolet and visible (UV-Vis) spectroscopy, Raman spectroscopy, and N_2 adsorption/desorption isotherms. The lowest sintering temperature (600°C) to obtain phase pure BZT powders with high surface area (14.5 m^2/g) has been determined from the thermal decomposition and phase analyses. The photocatalytic activity of the BZT powders has been tested for the decolorization of organic azo-dye and found to be photoactive under UV irradiation. The electronic band structure of the BZT has been investigated using density functional theory (DFT) calculations to determine the band gap energy (3.12 eV) and to compare it with experimental band gap (3.02 eV at 800°C) from optical absorption measurements. An excellent match is obtained for an assumption of Zn cation substitutions at specifically ordered sites in the BZT structure.

1. Introduction

Mixed metal pyrochlore oxides containing TiO_6, NbO_6, or TaO_6 octahedral units have been extensively studied in the past few years as a new class of photocatalysts [1–3]. For example, Bi-based pyrochlores, such as $Bi_2Ti_2O_7$, Bi_2MNbO_7 (M=Al, Fe, In, Sm), and Bi_2MTaO_7 (M=Al, Ga, In, Fe), have received significant attention in photocatalytic research [3–5]. More recently, another type of Bi-based pyrochlore material, Cu doped $Bi_{1.5}ZnTa_{1.5}O_7$ prepared by conventional powder processing method in thick-film form, has also been examined for photocatalytic water splitting [6].

In general, 3*d*-transition metals have commonly been used as dopants for wide band gap photocatalysts, in attempts to narrow their band gaps [7, 8]. Several of these attempts have aimed at developing visible-light sensitive photocatalysts out of the initial UV light responsive semiconductors. For instance, metal ions, such as Ni^{2+} and Cu^{2+}, have been doped into $InTaO_4$ and $BiTaO_4$ semiconductors, respectively [9, 10].

It has been hypothesized that the band gap value could be narrowed by raising the top of the valence bands due to the higher occupied M 3*d* orbitals of the dopants than O 2*p* orbitals [11]. However, many of the above-mentioned investigations have often been experimentally driven and have not been matched with a corresponding level of detailed electronic band structure calculations. For example, there are limited reports in the literature about the effect of M^{2+} *d*-block transition metal dopants, such as Zn^{2+}, Cu^{2+}, Ni^{2+}, or Co^{2+}, on the energy band structure of the pyrochlore materials.

We have recently investigated the properties and photocatalytic activity of BZN materials both experimentally and theoretically using density functional theory (DFT) calculations. Conditions for good match between theoretical calculations and experimental results have been identified.

In this paper, the phase evolution of BZT prepared by sol-gel synthesis has been characterized to determine the optimum temperature for phase pure formations and for optimized physical properties. The photocatalytic ability of the BZT powders has been tested for the decolorization of azo-dye aqueous solution under UV irradiation. Optical properties have been characterized by optical absorption spectroscopy and estimated experimental band gaps have been used as reference for comparison with calculations of the electronic band structure using DFT.

2. Experimental Procedure

2.1. Material. Bismuth acetate ($Bi(CH_3COO)_3$), tantalum ethoxide ($Ta(OC_2H_5)_5$), and zinc acetate dihydrate ($Zn(CH_3COO)_2{\cdot}2H_2O$) have been selected as sources of Bi, Ta, and Zn, respectively. Solvents, such as 1,3-propanediol ($CH_2(CH_2OH)_2$) and acetic acid ($C_2H_4O_2$), have been used as complexing agents during synthesis. All these chemicals are of analytical grade (≥99.9%) and have been purchased from Aldrich (Australia). These starting materials have been used according to the required stoichiometric ratio to prepare cubic BZT with $Bi_{1.5}ZnTa_{1.5}O_7$ composition. The details of synthesis process have been described in our previous publication [12].

2.2. Characterization. Thermal analyses have been carried out on a viscous gel sample, which had been previously prepared at 200°C from the liquid suspension of precursors, using thermogravimetric analysis (TGA) coupled with mass spectrometry (MS) and infrared emission spectrometry (IES). The results have been used to determine the lowest temperature to form organic free powders. X-ray diffraction (XRD), ultraviolet-visible (UV-Vis) spectroscopy, Raman spectroscopy, and N_2 adsorption/desorption isotherms have been employed to characterize further the powder samples prepared at various temperatures.

2.3. Photocatalytic Reaction. The photocatalytic ability of the BZT powders for the decolorization of azo-dye aqueous solution has been tested using UV light irradiation. A starting 20 ppm solution of acid orange 7 (AO7), dispersed with 0.1 g of powders, has been used in the reaction. The diminishing concentration of the AO7 dye has been monitored by UV-Vis spectroscopy, recording its maximum absorption peak (λ_{max}) at a wavelength of *ca*. 485 nm, in the visible-light region. The light source used in this experiment is 15 W NEC black light FL15BL (wavelength of *ca*. 365 nm).

3. Theoretical Calculations

3.1. $Bi_{1.5}ZnTa_{1.5}O_7$ Structure. The crystal structures of BZT used in DFT calculations have been taken or adapted from the Crystallographic Information File (CIF) of the Inorganic Crystal Structure Database (ICSD) for BZT. Cubic BZT from the CIF file (JCPDS PDF, 04-013-6484) has a lattice parameter a = 10.54 (Å) and contains fractionally occupied cations with ratios of Bi/Zn = 75 : 25 and Ta/Zn = 75 : 25 in the *A* and *B* sites, respectively. This random, fractionally occupied, solid solution structure has also been modified to ordered (completely and partially) solid solution, by making all or some of the Zn substitutions at specific sites of the structure, respectively.

Figure 1(a) shows a schematic of the random solid solution. Atoms are displayed using a ball and stick style, where mixed cations of Bi/Zn and Ta/Zn are orange and purple balls, respectively, and pure O anions are green balls. An example of the BZT (completely) ordered solid solution is displayed in Figure 1(b). This example results in the most representative and consistent calculations with experimental results. In the case for ordered solid solution, yellow, blue, and green balls are pure Bi, pure Ta cations, and pure O anions, while red balls are substituted Zn cations at the *A* and *B* sites, respectively. In the case for partially ordered BZT solid solution structures, the Zn substitution at either the *A* or the *B* sites is randomly substituted, while the other site is ordered, or vice versa.

3.2. Electronic Structure Calculations. The energy band structure and density of states (DOS) of the BZT compound have been calculated using DFT, as implemented in the Cambridge Serial Total Energy Package (CASTEP) of Materials Studio 8.0. In all calculations, the structures have been geometry and cell optimized. Both the local density approximation (LDA) with Ceperley and Alder exchange correlation functional parametrized by Perdew and Zunger (CP) and the generalized gradient approximation (GGA) with Perdew-Burke-Ernzerhof (PBE) functionals with norm-conserving pseudopotentials have been used along with setups nonmetal, nonspin and 100 empty orbitals. For random solid solutions, the ultrafine convergence tolerance setup has been used with k-grid of 0.03 A^{-1}, which gives k-point mesh of 6 × 6 × 6 and plane wave basis set cut-off of 830 eV.

In the case of ordered solid solutions, for the calculations to achieve convergence, default criteria have been customized to less demanding values than what is used for the random solid solution calculations. Final convergence has been achieved with customized tolerance setups for energy = 5.0×10^{-5} eVatoms^{-1}, force = 0.03 eVÅ^{-1}, stress = 0.02 GPa, and displacement = 5.0×10^{-3} Å, respectively, with k-grid of 0.07 A^{-1}, which gives a k-point mesh of 2 × 2 × 2 and plane wave basis set cut-off energy of 750 eV. Moreover, for the partially ordered solid solutions, fine convergence default setups for energy = 1.0×10^{-5} eVatoms^{-1}, force = 0.03 eVÅ^{-1}, stress = 0.05 GPa, and displacement = 1.0×10^{-3} Å, respectively, with k-grid of 0.03 A^{-1}, which gives a k-point mesh of 4 × 4 × 4 and cut-off energy of 750 eV, have been successfully used in the calculation.

4. Results and Discussion

4.1. Thermal Decomposition Analysis. The thermogravimetric (TG) and differential thermogravimetric (DTG) curves of the gel sample are shown as dash and solid lines in Figure 2, respectively. TGA analysis shows that the decomposition of the gel sample can be divided into three main mass loss

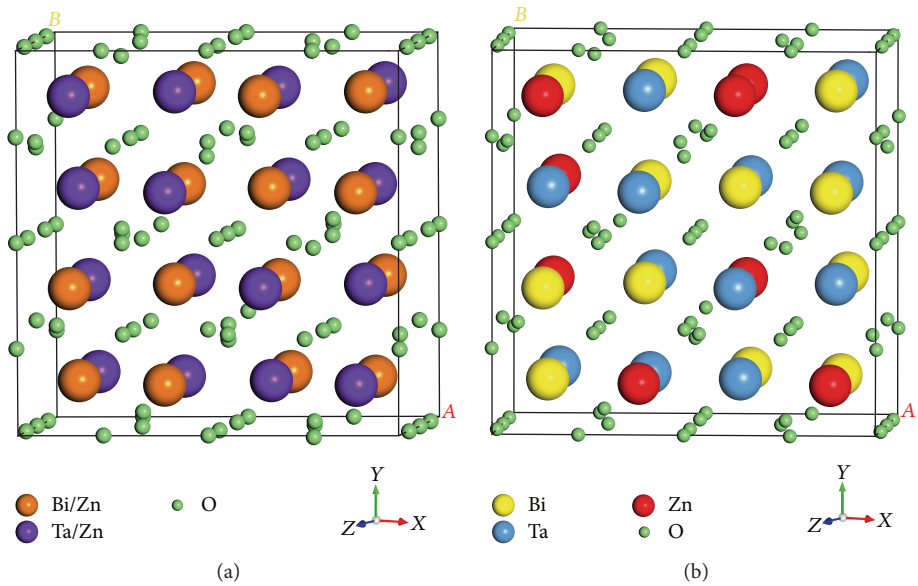

Figure 1: BZT structures assuming (a) random and (b) ordered solid solutions (pure Bi, Ta, Zn, and O are yellow, blue, red, and green balls, while Bi/Zn and Ta/Zn mixed cations are orange and purple balls, resp.).

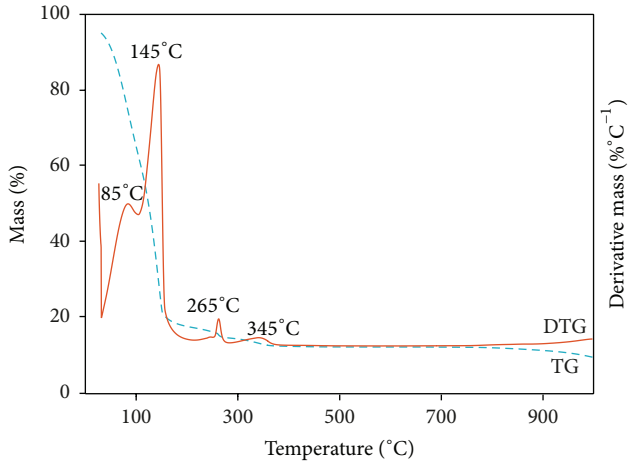

Figure 2: TG/DTG curves of the gel sample that heated from 25 to 1000°C.

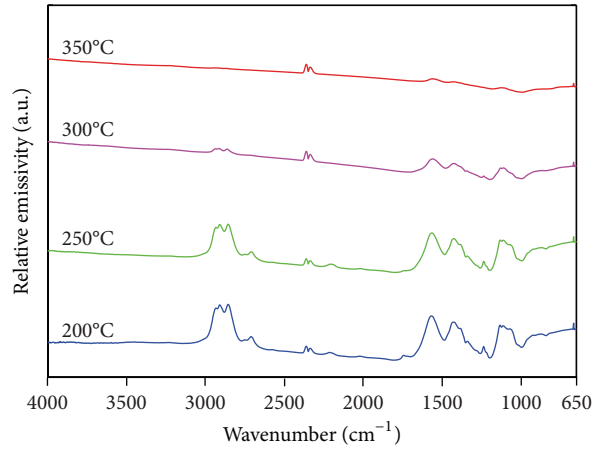

Figure 3: IES spectra of the gel sample heated at various temperatures.

events, which correspond to the peaks observed at 85–145, 265, and 345°C in the DTG curve and to 80, 5, and 3% of the total mass loss, respectively. With further increases in heating temperature up to 800°C, no significant additional mass loss has been observed, which may be an indication of no volatility of metallic Bi or any other metals.

4.2. IES Analysis. The IES spectra collected in the range of 650–4000 cm^{-1} from the gel sample while heating from 200 to 350°C on the platinum nail surface used in the IES experiments are shown in Figure 3. Absorption peaks have appeared at various wavenumbers for the sample heated at 200°C. These peak intensities have noticeably decreased with increasing temperature up to 300°C, and most of these peaks have then disappeared from 350°C onwards.

Bands between 2700 and 2800 cm^{-1} and 1450–1475 cm^{-1} are due to saturated –C–H stretching and deformations found in the form of $-CH_2$ and $-CH_3$, respectively. The peaks obtained at 2700–2800 cm^{-1} are due to either –O–CH_3 or –O–CH_2–O– groups, while a small peak at 3200–3550 cm^{-1} may correspond to –OH groups. A single sharp peak associated with saturated ester or carboxylic acid –CO–O bonds at about 1735–1750 cm^{-1} has also been observed in the spectra. Moreover, broad peaks of –C–C, –C–O, and –C=C stretches are also found in the regions around 1000, 1300, and 1640 cm^{-1}, respectively. CO_2 peaks appear at 2350 cm^{-1} at all temperatures due to the experiment being carried out in

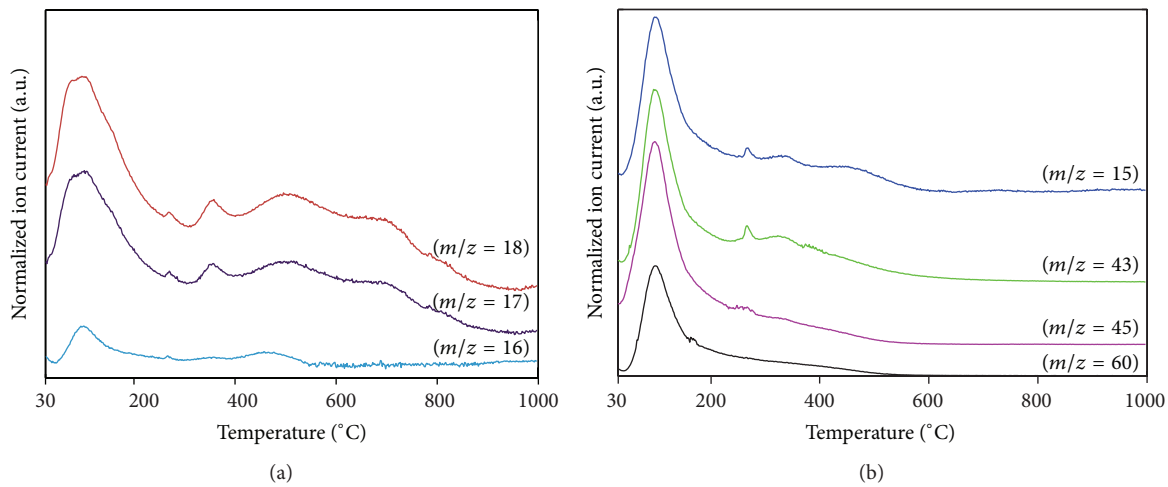

Figure 4: Ion currents in the MS curves, (a) water and (b) organics.

ambient air. This result indicates that the organic compounds in the precursors have completely decomposed before the powders form at 350°C, which is in agreement with the TGA results.

4.3. MS Analysis. The detected ion currents of evolved gasses from the thermal decomposition of the gel sample are well matched with the evolution of water and fragmentation of organic compounds at particular decomposition temperatures. The water dehydration has occurred at several different event temperatures in the forms of O ($m/z = 16$), OH ($m/z = 17$), and H_2O ($m/z = 18$) as shown in Figure 4(a). The vaporization of large amount of water takes place at about 100°C and it is probably the result of dehydration of zinc acetate dihydrate or reaction between organic solvents during the synthesis process [13]. Small amounts of higher temperature water dehydration at 270, 355, and 500°C have also been observed in the MS curves.

Figure 4(b) illustrates the sharp peaks obtained in the ion current curves at 100°C, which may be assigned to CH_3 ($m/z = 15$), CH_3CO ($m/z = 43$), COOH ($m/z = 45$), and CH_3COOH ($m/z = 60$). These peaks could be the result of a vaporization of an excess of organic solvents in the gel sample, such as acetic acid, propanediol, or other organics. Additional organic decompositions are observed at 270 and 335°C, which may correspond to the elimination of remaining organic radical groups polymerized with the metals and subsequently allowing the crystallization of organic free –Bi–O–Zn–O–Ta– metal oxide mixture.

4.4. SEM Analysis. Figure 5 shows the backscattered SEM images of the gel and powder samples prepared at different temperatures. The uniformity of the contrast indicates that the elemental distribution of the microparticles is relatively homogeneous.

The SEM micrograph in Figure 5(a) illustrates the long-sheet like porous gel sample that consists of small clusters with a thickness of 500–700 nm. Figures 5(b) and 5(c) show the SEM micrographs of powder samples prepared at 400 and 600°C, which consist of particles of 0.5 and 20 μm sizes, respectively. At higher temperatures, grain growth is observed and the powders develop a dense microstructure with large clusters in the form of >5 μm thick plates, exceeding 30 μm diameters when the sample is heated at 800°C as shown in Figure 5(d).

4.5. XRD Analysis. X-ray diffraction has been employed to identify the crystalline phases at various sintering temperatures. Diffraction patterns of thermally treated powders prepared at 400–800°C are shown in Figure 6. The compounds obtained at the lower temperatures of 400 and 500°C corresponding to a mixture of intermediate phases are identified as $Bi_{7.84}Nb_{1.61}O_{14.78}$ in the database.

With an increase of sintering temperature, however, single phase BZT crystals are obtained at 600°C onwards. All the main peaks can be matched to those of cubic $Bi_{1.5}ZnTa_{1.5}O_7$ (JCPDS PDF, 04-013-6484). The peak widths become narrow with increasing temperature, indicating higher crystallinity. BZT crystallite sizes calculated from the Scherrer equation are 32–48 nm at 600–800°C, respectively.

XPS analysis has been carried out on the powder sample sintered at 800°C. The surface composition of the BZT has been calculated based on atomic ratio of each metal in the compound. The peak areas of Bi 4*f* (at 159 and 165 eV), Zn 2*p* (at 1021.68 eV), and Ta 4*f* (at 26.5 and 27.5 eV) have been measured, and quantification of the peaks gives the atomic ratio of Bi : Zn : Ta to be approximately 1.6 : 1 : 1.7 on the surface of the BZT pyrochlores. The XPS results have also confirmed that the oxidation states of each cation are Bi^{3+}, Zn^{2+}, and Ta^{5+}, respectively, at that temperature.

4.6. Raman Spectrometry Analysis. Raman spectrometry in the wavenumber range of 100–1000 cm^{-1} has confirmed the XRD results for the phase formations at various temperatures. Figure 7(a) presents Raman spectra collected on a gel sample prepared at 200°C and on powder samples heated at 400 and

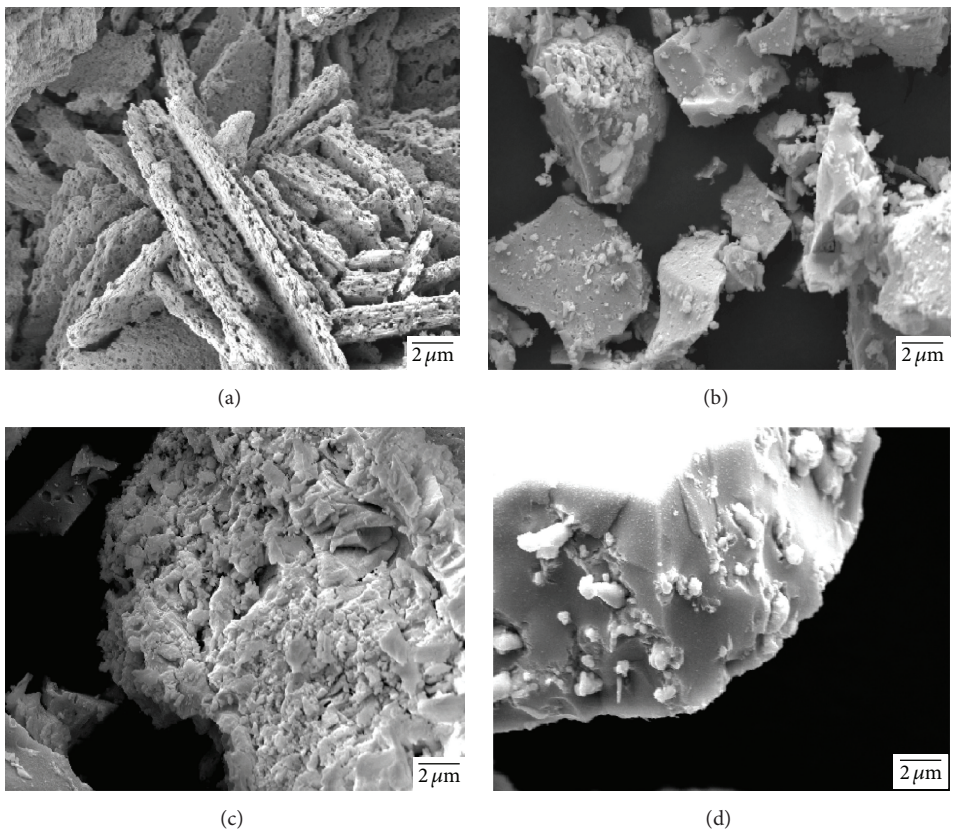

Figure 5: SEM images of samples prepared at (a) 200°C, (b) 400°C, (c) 600°C, and (d) 800°C (all images have same scale of 2 μm).

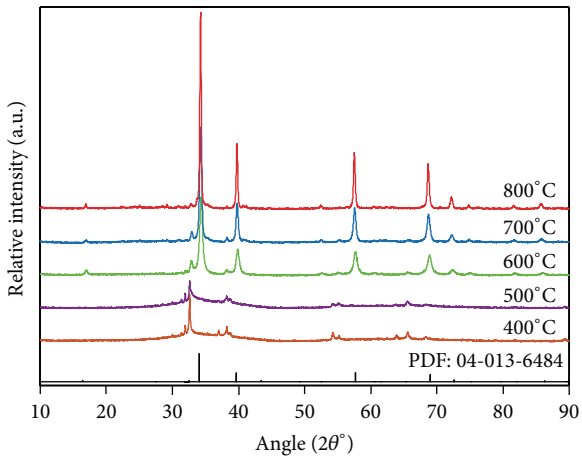

Figure 6: XRD patterns of powder samples prepared at various temperatures (the bottom pattern is the cubic BZT with PDF card number).

500°C, respectively. The changes in relative peak heights and positions show the occurrence of a phase transformation. Two intense and narrow peaks at 186 and 316 cm^{-1} and three small shoulder peaks at 466, 635, and 787 cm^{-1} are found on the Raman spectra from the powders prepared at 500°C. These peaks are probably due to the intermediate oxides identified using XRD analysis.

Raman spectra of the powder samples sintered at 600–800°C are displayed in Figure 7(b). The peaks obtained at 285, 445, 557, 615, and 745 cm^{-1} at all temperatures that consist of broad bands and shoulders are closely matched with those published for BZT in the literature [14]. However, the peaks found at 135, 150, and 235 cm^{-1} are not reported in previous work; the spectra were collected between 250 and 1000 cm^{-1} only. With increasing temperature from 600 to 800°C, the peak positions remain unchanged; yet, the features become more pronounced, which is probably due to larger sized grains and particles formed at higher temperature.

4.7. UV-Vis Spectroscopy Analysis. Figure 8 displays the optical absorption edges of BZT powders prepared at various temperatures. The absorption curves at 400 and 500°C clearly show that samples consist of a mixture of different phases. However, at higher sintering temperature, single phase BZT powders show optical absorptions at wavelengths about 410–450 nm in the UV light region. The estimated optical band gaps of cubic BZT compounds obtained at 600, 700, and 800°C are about 2.75, 2.95, and 3.02 eV, respectively, which is comparable to previously reported values of 2.5–3.2 eV in the literature [14].

4.8. Photocatalytic Dye Decolorization. The photocatalytic activity of the BZT compound has been evaluated for the decolorization of AO7 solution under UV irradiation for

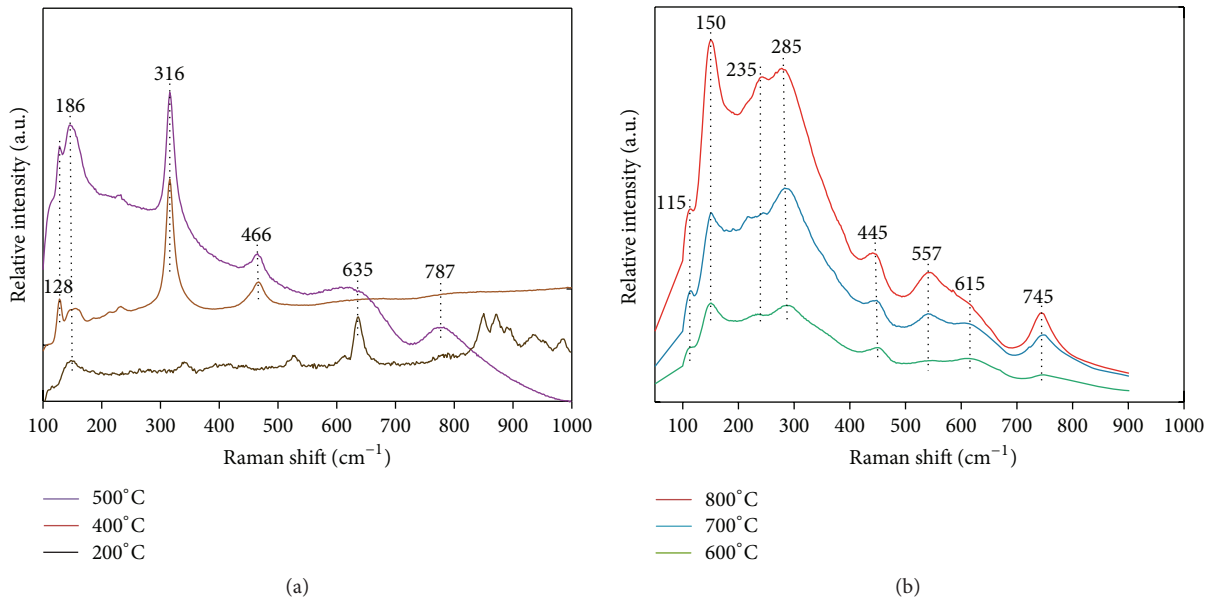

Figure 7: Raman spectra of samples prepared at various temperatures.

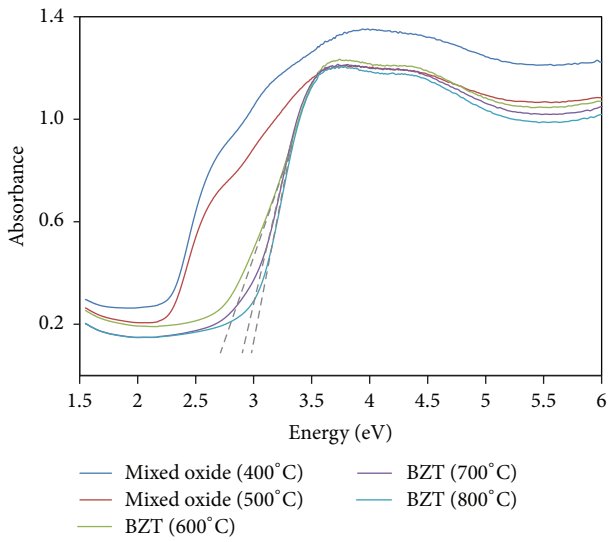

Figure 8: UV-Vis spectra of powder samples prepared at various temperatures.

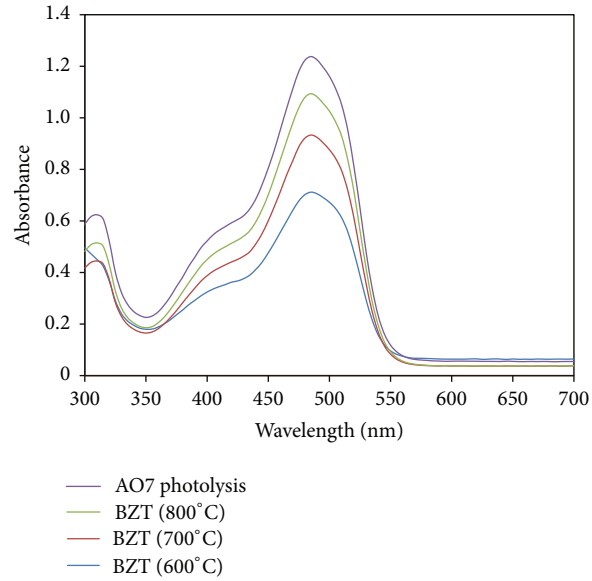

Figure 9: AO7 dye absorption curves (λ_{max} = 485 nm) after photocatalytic degradation for 60 min under UV irradiation in the presence of the BZT catalysts prepared at various temperatures.

60 min. Figure 9 shows the changes in the dye concentration in the presence of BZT powders prepared at 600–800°C. The results indicate that BZT is photoactive under UV light with wavelength of *ca.* 365 nm and that the photocatalytic degradation of the azo-dye in aqueous media is achieved with assistance of the BZT catalyst, photoexcited by UV irradiation. As expected, the low temperature catalyst at 600°C has shown better performance than higher temperature catalysts, which correlates with its higher surface area (14.5 m^2/g) when compared to that of BZT powders prepared at 800°C (0.47 m^2/g). These results are similar to our previous photocatalysis results using BZN powders.

4.9. Electronic Structure Calculations. All attempts to calculate the electronic band structure of the BZT with complete fractional occupancy have resulted in metallic-like materials without band gaps near or from the Fermi level. The lattice parameter of this calculated cubic structure is a = 10.22 Å. These results have been consistent for all different settings (k-grid, cut-off energy, spin-polarized or unpolarized options, etc.) for both cubic and primitive structures used in the calculations.

The calculated results obtained from the DOS for BZT random solid solution have revealed that the bands near

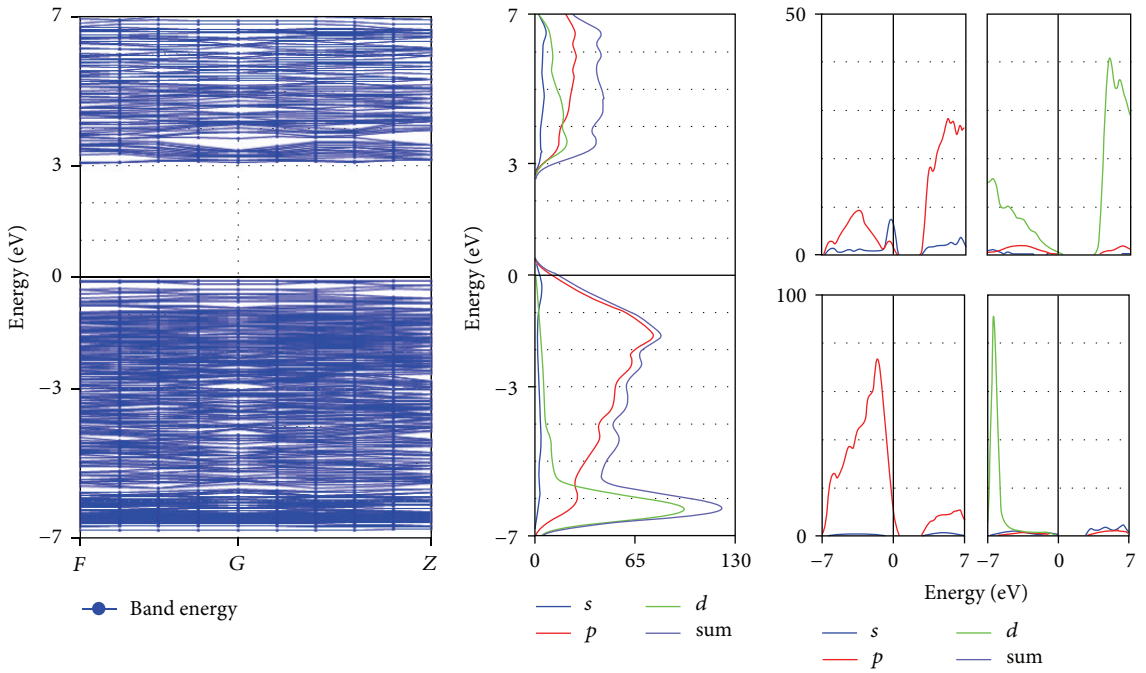

(a) Band structure

(b) Density of states

Figure 10: The band structure and DOS for the BZT ordered solid solution structure.

the Fermi level contain mainly d and a small amount of p orbitals. Supplementary calculations with gradual amounts of Zn substituted in the structures have shown that these bands arise mainly from Ta 5d orbitals that are driven downwards in energy by the involvement of Zn cations in the B site of the BZT structure. Fractional occupancy of Zn in the A sites does not show such a marked effect. Since this has not reflected the experimentally observed optical results, completely and partially BZT ordered solid solutions have also been explored in the DFT studies.

The electronic structure and DOS calculations for the BZT ordered solid solution are shown in Figure 10. After the calculations, the cubic structure (a = 10.54 Å) has been slightly contracted and converted to rhombohedral structure with lattice parameter a = 10.42 Å and angles of 90.13°, which clearly represents a very small distortion from the input cubic structure. The obtained final enthalpy of formation of −58449.02 eV for the BZT ordered solid solution is generally lower than the enthalpy of formation of −55972.85 eV for the cubic BZT random solid solution, which is generally taken as an indication of favourable formation. Figure 10(a) shows a band gap, which is calculated as 3.12 eV between the dense VB and CB bands, which compares very well with experimentally estimated band gaps of 2.75–3.02 eV for optical absorption measurements.

Figure 10(b) shows the total and partial DOS for overall BZT and individual atoms, respectively. The VB bands mainly consist of O 2p, Bi 6s, Bi 6p, and Ta 5d states, whereas the CB bands consist mainly of Ta 5d, Bi 6p, and O 2p states. With respect to the contribution of Zn to the energy band structure, a pronounced peak of 3d states is obtained between −5.5 and −7.0 eV. This energy level is several eVs below the Fermi level and it may therefore only contribute indirectly to the determination of the size of the band gap.

The partially ordered solid solution, in the A and B sites, produced calculated band structures that more closely matched the experimental results. The lattice parameter of this calculated cubic structure is a = 10.44 Å and the band gap is 1.86 eV. In addition to the continuous bands, the calculation for the partial solid solution also appears to show a few localized bands inside the band gap. These bands seem to be impurity bands, which are due to Zn s orbitals in both VB and CB levels as a result of mixed Bi/Zn cations in the random solid solution. Such impurity bands may act as traps for photogenerated electrons or holes during the photocatalytic reaction. The dense groups of states at the VB and the CB above the localized bands are separated by about 3.5 eV, which corresponds to the optical absorption edge. This value is slightly higher than the experimentally determined absorption edge and the value obtained for the completely ordered solid solution calculations.

In contrast, when Zn is randomly substituted in the A and ordered in the B sites, the electronic band structure calculation results show no band gap, which is similar to the calculated results from the random solid solution (for the unpolarized case). In this case, Ta d orbitals are driven downwards in energy by the involvement of Zn cations in the B site of the BZT structure as Ta/Zn mixed random cations.

5. Conclusions

Single-phased cubic BZT has been successfully synthesized using an alkoxide based sol-gel reaction route. The lowest temperature required for phase purity and maximum surface

area has been determined to be around 600°C through the characterization of the phase evolution from the alkoxide precursors as function of temperature. The BZT has been found to be UV light responsive, as determined from the photocatalytic degradation of azo-dye in aqueous solution. Band gaps of 2.75–3.02 eV have been estimated from optical absorption measurements and have been used as reference for detailed DFT investigations of the electronic band structure, assuming both random and ordered solid solutions. Random solid solutions, which correspond to CIF files generated from refinements of XRD patterns, have resulted in complete absence of electronic band gaps. This is the case whether unpolarized or polarized spins are assumed. To obtain an electronic band gap, ordered solid solutions have been required. A selected ordered solution has resulted in a calculated band gap of 3.12 eV, which appears clean, without impurity bands and matches very well the experimentally estimated band gaps. It should be noted that this choice of substitution results in reduction of the symmetry to rhombohedral after geometry optimization. By choosing a partially ordered solid solution, a slightly larger band gap can be obtained while retaining the cubic symmetry after geometry optimization.

Conflict of Interests

The authors declare that there is no conflict of interests regarding the publication of this paper.

Acknowledgments

The authors are thankful for Queensland University of Technology (QUT) for research facility support. They would also like to thank the staff from the QUT Central Analytical Research Facility (CARF), Dr. Llew Rintoul and Mr. Adrian Backer, for their help during some of the data collections.

References

[1] Z. Zou, J. Ye, and H. Arakawa, "Structural properties of $InNbO_4$ and $InTaO_4$: correlation with photocatalytic and photophysical properties," *Chemical Physics Letters*, vol. 332, no. 3-4, pp. 271–277, 2000.

[2] B. Muktha, J. Darriet, G. Madras, and T. N. Guru Row, "Crystal structures and photocatalysis of the triclinic polymorphs of $BiNbO_4$ and $BiTaO_4$," *Journal of Solid State Chemistry*, vol. 179, no. 12, pp. 3919–3925, 2006.

[3] W. F. Yao, H. Wang, X. H. Xu et al., "Photocatalytic property of bismuth titanate $Bi_2Ti_2O_7$," *Applied Catalysis A: General*, vol. 259, no. 1, pp. 29–33, 2004.

[4] L. M. Torres-Martinez, I. Juarez-Ramirez, J. S. Ramos-Garza, F. Vazquez-Acosta, and S. W. Lee, "Bi_2MTaO_7 (M = Al, Fe, Ga, In) photocatalyst for organic compounds degradation under UV and visible light," *WSEAS Transactions on Environment and Development*, vol. 6, no. 4, pp. 286–295, 2010.

[5] L. L. Garza-Tovar, L. M. Torres-Martínez, D. B. Rodríguez, R. Gómez, and G. Del Angel, "Photocatalytic degradation of methylene blue on Bi_2MNbO_7 (M = Al, Fe, In, Sm) sol-gel catalysts," *Journal of Molecular Catalysis A: Chemical*, vol. 247, no. 1-2, pp. 283–290, 2006.

[6] J. Sun, G. Chen, J. Pei, R. Jin, and Y. Li, "A novel $Bi_{1.5}Zn_{1-x}Cu_xTa_{1.5}O_7$ photocatalyst: water splitting properties under visible light and its electronic structures," *International Journal of Hydrogen Energy*, vol. 37, no. 17, pp. 12960–12966, 2012.

[7] A. Hameed, M. A. Gondal, and Z. H. Yamani, "Effect of transition metal doping on photocatalytic activity of WO_3 for water splitting under laser illumination: role of 3*d*-orbitals," *Catalysis Communications*, vol. 5, no. 11, pp. 715–719, 2004.

[8] Z. Zou, J. Ye, R. Abe, K. Sayama, and H. Arakawa, "Effect of 3*d* transition-metal (M) doping in $In_{1-x}M_xTaO_4$ photocatalysts on water splitting under visible light irradiation," *Studies in Surface Science and Catalysis*, vol. 145, pp. 165–168, 2002.

[9] Z. Zou, J. Ye, and H. Arakawa, "Effect of Ni substitution on the structure and photocatalytic activity of $InTaO_4$ under visible light irradiation," *Journal of Materials Research*, vol. 17, no. 6, pp. 1419–1424, 2002.

[10] H. Zhang, G. Chen, X. Li, and Q. Wang, "Electronic structure and water splitting under visible light irradiation of $BiTa_{1-x}Cu_xO_4$ (x = 0.00–0.04) photocatalysts," *International Journal of Hydrogen Energy*, vol. 34, no. 9, pp. 3631–3638, 2009.

[11] H. Tong, S. Ouyang, Y. Bi, N. Umezawa, M. Oshikiri, and J. Ye, "Nano-photocatalytic materials: possibilities and challenges," *Advanced Materials*, vol. 24, no. 2, pp. 229–251, 2012.

[12] G. Perenlei, P. C. Talbot, and W. N. Martens, "Sol-gel synthesis and characterization of cubic bismuth zinc niobium oxide nanopowders," *Journal of Nanomaterials*, vol. 2014, Article ID 695973, 6 pages, 2014.

[13] A. V. Ghule, K. Ghule, C.-Y. Chen et al., "In situ thermo-TOF-SIMS study of thermal decomposition of zinc acetate dihydrate," *Journal of Mass Spectrometry*, vol. 39, no. 10, pp. 1202–1208, 2004.

[14] S. M. Zanetti, M. G. S. Pereira, and M. C. A. Nono, "Soft-chemical derived Bi_2O_3-ZnO-Ta_2O_5 nanopowder and ceramics," *Journal of the European Ceramic Society*, vol. 27, no. 13–15, pp. 3647–3650, 2007.